

# Modal analysis of high-fidelity simulations in turbomachinery

Christian Morsbach, Bjoern F. Klose, Michael Bergmann, and Felix M. Möller

**Abstract** We revisit recently published high-fidelity implicit large eddy simulation datasets obtained with a high-order discontinuous Galerkin spectral element method and analyse them using Proper Orthogonal Decomposition (POD) as well as Spectral Proper Orthogonal Decomposition (SPOD). The first configuration is the MTU T161 low-pressure turbine cascade with resolved end wall boundary layers in a clean version and one with incoming turbulent wakes. We focus on the behaviour of the laminar separation bubble and the secondary flow system and how these phenomena are affected by incoming wakes. The second configuration is a transonic compressor cascade in which we analyse the unsteady behaviour of the shock wave boundary layer interaction. Throughout the paper, we try to discuss not only the flow physics but also insights into how the modal decomposition techniques can help facilitate understanding and where their limitations are.

---

Christian Morsbach  
Institute of Propulsion Technology, German Aerospace Center (DLR), Cologne, Germany, e-mail: christian.morsbach@dlr.de

Bjoern F. Klose  
Institute of Test and Simulation for Gas Turbines, German Aerospace Center (DLR), Cologne, Germany, e-mail: bjoern.klose@dlr.de

Michael Bergmann  
Institute of Propulsion Technology, German Aerospace Center (DLR), Cologne, Germany, e-mail: michael.bergmann@dlr.de

Felix Möller  
Institute of Test and Simulation for Gas Turbines, German Aerospace Center (DLR), Cologne, Germany, e-mail: felix.moeller@dlr.de

## 1 Introduction

Computational Fluid Dynamics (CFD) simulations have revolutionized our ability to predict and understand complex flow phenomena. With increasing computing resources and the development of high-order methods, simulations produce more and more high-fidelity datasets, which are difficult to analyse. While these datasets have the potential to improve our understanding of flow physics, the sheer amount of data, and its temporal and spatial resolution, make gaining insights a challenging task. Hence, most Large Eddy Simulation (LES) studies only discuss time-averaged quantities or features based on snapshots.

To facilitate the analysis of these datasets, researchers have recently developed data analysis techniques, such as Proper Orthogonal Decomposition (POD) [5, 20], Spectral Proper Orthogonal Decomposition (SPOD) [16], and Dynamic Mode Decomposition (DMD) [15], which have gained significant attention in the computational fluid dynamics community. These methods allow for the extraction of the most energetic modes (POD) and sorting by frequency content (SPOD).

Traditionally, these modal decomposition techniques have been applied to experimental data. Some recent examples include POD of Particle Image Velocimetry (PIV) data from a centrifugal compressor inlet [3], POD and DMD applied to analyse PIV data of a laminar separation bubble undergoing transition to turbulence [12, 1, 7], POD used to investigate the interaction of high- and low-pressure turbine based on unsteady total pressure data in planes between the blade rows [2], or an investigation of transonic buffet using DMD of PIV data [8]. Very early numerical studies were based on unsteady Reynolds-averaged Navier-Stokes (RANS) data, e.g. [6], but more recently, turbulence resolving approaches such as hybrid RANS/LES or LES have become feasible. Fiore *et al.* [9] recently applied the SPOD method to a low-pressure turbine flow with laminar inflow, as well as with wakes generated by a row of upstream cylinders. They found that the cylinder wakes amplify certain modes over the blade and increases turbulence downstream of the trailing edge over a reduced frequency bandwidth. Mechanisms of trailing edge (TE) cutback film cooling flows at different blowing ratios have been investigated using SPOD on Delayed Detached Eddy Simulation (DDES) data by Wang *et al.* [19]. Here, the authors analysed how the structure of vortex shedding changes with blowing ratio. He *et al.* [10] recently presented an extensive analysis of the compressor tip leakage flow using SPOD on data obtained with a DDES. They used the complete 3D flow field in the tip region of the blade as input for the SPOD and identified low-rank behaviour over a range of frequencies associated with an oscillation of the tip leakage vortex and vortex shedding after its breakdown.

At the German Aerospace Center (DLR), we generate LES data with a numerical test rig for turbomachinery based on the high-order Discontinuous Galerkin Spectral Element Method (DGSEM). In this study, we will reconsider previously published high-fidelity datasets of turbomachinery flows [11, 14] generated with our DGSEM solver TRACE [4] and extract the dominant dynamic features using POD and SPOD. The datasets include the interaction of wakes with downstream low-pressure turbine blades and the shock boundary layer interaction in a compressor cascade. The study

will discuss the advantages and limitations of each method and provide insights into how these techniques can be used to gain a deeper understanding of complex flow phenomena.

## 2 Modal decomposition techniques

In this section, we will very briefly introduce POD and SPOD to clarify the terminology.

### 2.1 Proper Orthogonal Decomposition (POD)

POD by itself is not a new method. Its theoretical background and formulation have been reviewed decades ago [5]. The formulation here is inspired by the review of Schmidt and Colonius [16] as well as the tutorial by Weiss [20]. For a consistent derivation of how a snapshot POD can be conveniently computed on non-equidistant grids using a Singular Value Decomposition (SVD), we refer the interested reader to the appendix.

We define the matrix of  $M$  snapshots of fluctuating quantities (mean subtracted) where each snapshot is a row and spatial dimensions as well as multiple variables are flattened to size  $N$ :

$$\mathbf{X} = \begin{pmatrix} - & \mathbf{x}_1^H & - \\ & \vdots & \\ - & \mathbf{x}_M^H & - \end{pmatrix} \in \mathbb{C}^{M \times N}. \quad (1)$$

The POD is based on the sample covariance matrix

$$\mathbf{C} = \frac{1}{M-1} \mathbf{X}^H \mathbf{X} \in \mathbb{C}^{N \times N} \quad (2)$$

through an eigenvalue problem with a weight matrix  $\mathbf{W}$  and inner product  $\langle \mathbf{x}_1, \mathbf{x}_2 \rangle = \mathbf{x}_1^H \mathbf{W} \mathbf{x}_2$  [16]:

$$\mathbf{C} \mathbf{W} \mathbf{\Phi} = \mathbf{\Phi} \mathbf{\Lambda}, \quad \mathbf{W} = \text{diag}(w_1, \dots, w_N). \quad (3)$$

Here,  $\mathbf{\Phi} \in \mathbb{C}^{N \times M}$  is the matrix of POD modes or eigenvectors and  $\mathbf{\Lambda} = \text{diag}(\lambda_1, \dots, \lambda_M)$  is the matrix of eigenvalues. The modes are orthonormal under the scalar product defined above:

$$\mathbf{\Phi}^H \mathbf{W} \mathbf{\Phi} = \mathbf{1}. \quad (4)$$

A linear combination of the modes to recover the original snapshots:

$$\mathbf{X} = \mathbf{A} \mathbf{\Phi}^T = \sum_j a_{ij} \mathbf{\Phi}_{jk} = \sum_j \tilde{\mathbf{X}}_j \in \mathbb{R}^{M \times N}. \quad (5)$$

This can be interpreted as sum of modal contributions with the time coefficients determined by

$$\mathbf{A} = \mathbf{X}\mathbf{W}\mathbf{\Phi} \in \mathbb{C}^{M \times N}. \quad (6)$$

## 2.2 Spectral Proper Orthogonal Decomposition (SPOD)

In this section, we briefly review the implementation of the SPOD algorithm based on Welch's periodogram method, which is used in this work. For a detailed description of the theoretical background, we refer the reader to Towne, Schmidt and collaborators [18, 16], as well as to Mengaldo & Maulik [13] for the implementation.

Just as done for the POD, we assemble the matrix of snapshots  $\mathbf{X}$  (1). Next, we apply Welch's spectral estimation method by decomposing the matrix along its time axis into  $N_{\text{blk}}$  overlapping blocks and, assuming that each realisation in the snapshot matrix occurs periodically in time, apply a discrete Fourier transform on each block after multiplication of the data by a Hamming window. The result is a set of  $N_{\text{blk}}$  Fourier transformed blocks  $\tilde{\mathbf{X}}_k$  with  $N_{\text{fft}}$  frequencies each.

For each frequency, we assemble the matrix  $\tilde{\mathbf{X}}$

$$\tilde{\mathbf{X}} = \begin{pmatrix} - & \tilde{\mathbf{x}}_1^H & - \\ & \vdots & \\ - & \tilde{\mathbf{x}}_{N_{\text{blk}}}^H & - \end{pmatrix} \in \mathbb{C}^{N_{\text{blk}} \times N}, \quad (7)$$

where, again,  $N$  is the number of spatial points times the number of variables and  $N_{\text{blk}}$  is the number of blocks. For each frequency, we compute the covariance matrix

$$\tilde{\mathbf{C}} = \frac{1}{N_{\text{blk}}} \tilde{\mathbf{X}}^H \tilde{\mathbf{X}} \in \mathbb{C}^{N \times N}, \quad (8)$$

and obtain the SPOD modes by solving the eigenvalue decomposition of the covariance matrix for each frequency separately [16]:

$$\tilde{\mathbf{C}}\mathbf{W}\mathbf{\Phi} = \mathbf{\Lambda}\mathbf{\Phi}, \quad \mathbf{W} = \text{diag}(w_1, \dots, w_N). \quad (9)$$

Here,  $\mathbf{W}$  is a weight matrix,  $\mathbf{\Phi}$  are the eigenvectors and  $\mathbf{\Lambda}$  the eigenvalues. Because the weight matrix is problem specific, we will discuss its form for each application separately.

## 3 Application to turbomachinery flows

In the following, we will apply both POD and SPOD to three different datasets with different flow phenomena. We will begin by investigating the transitional flow through the MTU T161 low-pressure turbine (LPT) with focus on separation-induced

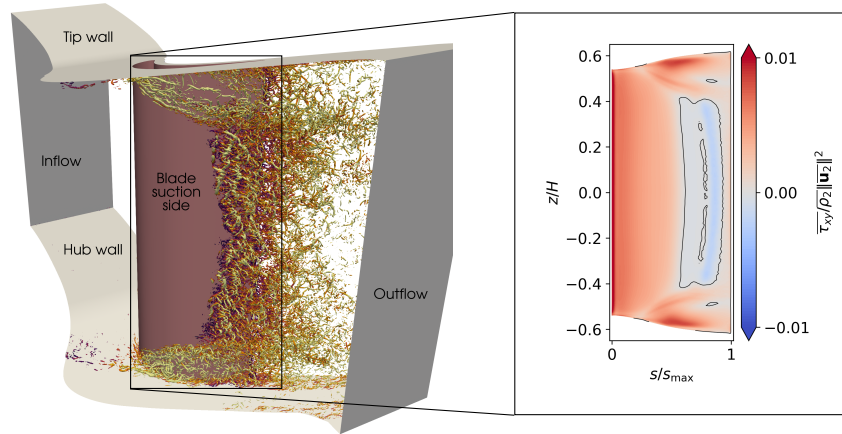


Fig. 1: Illustration of MTU T161 simulation domain with instantaneous vortex structures and mean in-plane wall shear stress  $\tau_{xy}$  on the blade suction side with  $\tau_{xy} = 0$  as black contour line

transition around midspan and large-scale unsteadiness of the secondary flow system. Additionally, we will analyse the influence of wakes from an upstream row. Finally, we will study shock wave boundary layer interaction in a linear compressor cascade.

### 3.1 Separation-induced transition and secondary flow effects

We analyse the turbulent flow through an LPT cascade at an off-design Reynolds number of 90 000 and a Mach number of 0.65 computed as implicit LES with a high-order DGSEM scheme [14]. We use a dataset containing the time-resolved wall shear stress vector on the blade suction side spanning 100 convective time units  $t_c$  based on chord length and outlet velocity with 3668 samples. The original sampling was 366 samples per  $t_c$  but we use only a tenth of that for the modal analysis, since that already covers the frequency range of interest. Fig. 1 shows the configuration with a view of the blade suction side of the configuration with instantaneous vortex structures visualised by the Q-criterion to illustrate the separation induced transition around midspan and the secondary flow regions close to the hub and tip walls. On the right-hand side, the mean in-plane wall shear stress  $\tau_{xy}$  on the blade suction side surface over the arc length from the leading edge (LE) at  $s = 0$  to the TE at  $s/s_{max} = 1$  is presented in the way we will display the mode shapes throughout this section. The  $z$  coordinate is normalised by the upstream channel height  $H$  allowing to see the diverging end walls. We will employ classical Fourier analysis, space-only POD and SPOD to investigate a potential connection between the Kelvin-Helmholtz (KH) based transition mechanism around midspan and oscillations of the corner flow.

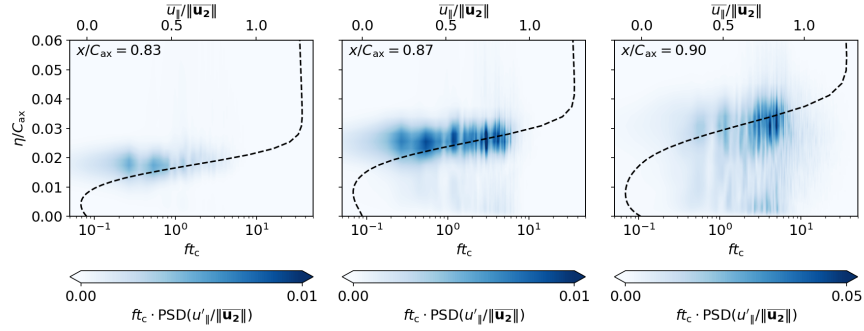


Fig. 2: Midspan premultiplied spectrum of  $u'_{||}$  for different distances  $\eta$  from the solid wall in boundary layer cuts of the MTU T161 blade suction side at  $x/C_{ax} = 0.83$  (pre-transitional),  $x/C_{ax} = 0.87$  (transition onset) and  $x/C_{ax} = 0.90$  (half way to fully turbulent)

In addition to the surface dataset, we use three wall-normal cuts through the suction side boundary layer at midspan to be able to relate frequencies to physical mechanisms in the flow. Fig. 2 shows premultiplied frequency spectra of the wall-parallel fluctuating velocity  $u'_{||}$  for these cuts varying with the distance from the solid wall. For orientation, the mean velocity profiles are plotted as black dashed lines. In the cut at  $x/C_{ax} = 0.83$ , where the separated shear layer is still laminar, only non-dimensional frequencies lower than 1 (time scales larger than a convective time unit) show noticeable content in the region of strongest shearing. Further downstream at  $x/C_{ax} = 0.87$ , where the flow begins its transition to turbulence, non-dimensional frequencies in the range 3-5 become excited due to the KH instability and have already surpassed the intensity found in the lower frequencies. These instabilities can be found to grow even further at  $x/C_{ax} = 0.90$ , where the maximum turbulent kinetic energy (TKE) in the boundary layer is at 50% of the maximum, reached slightly downstream. At this position, they dominate the whole spectrum and peaks at these frequencies can not only be found in the shear layer but also close to the solid wall. Observe the changed scale of the colourbar. We will find both the low frequency and high frequency effects in the modal analysis below.

Since our dataset has points clustered towards the leading and trailing edge, as well as towards the end walls, we use the element area as weights to perform a POD using an SVD with (14), (17) and (18). The input variables are the two independent components of the fluctuating wall shear stress vector  $\tau'_{xy}$  and  $\tau'_z$ , equally weighted using the weighted 2-norm [16]:

$$\mathbf{X} = [\tau'_{xy}, \tau'_z]^T, \quad \mathbf{W} = \int_V \text{diag}(dV, dV). \quad (10)$$

**Fig. 3** POD eigenvalues of MTU T161 suction side wall shear stress (*top*) and cumulative eigenvalues (*bottom*); values for Gaussian random data given as indication of noise threshold

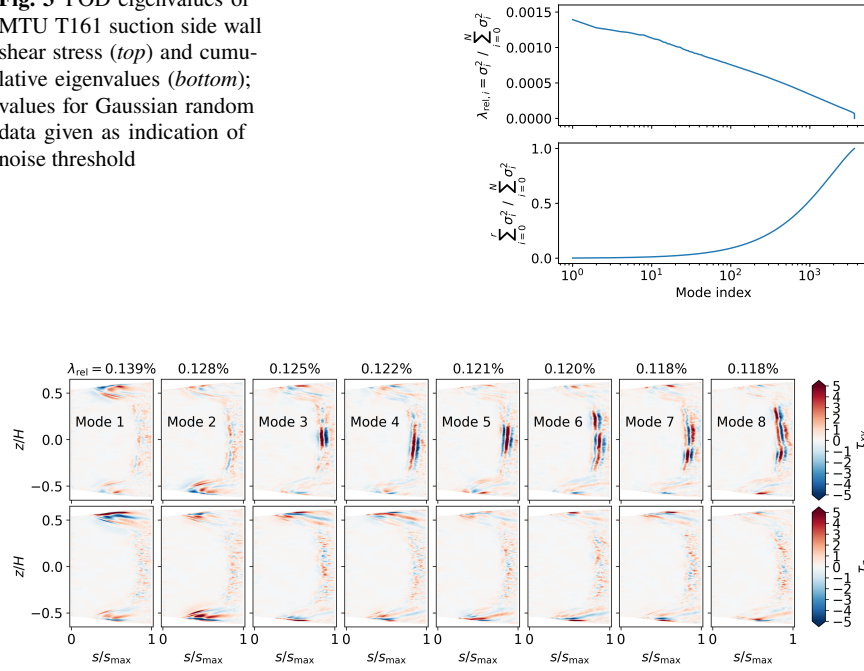


**Fig. 4:** MTU T161: First eight POD modes for in-plane (*top*) and spanwise (*bottom*) wall shear stress  $\tau_{xy}$ ,  $\tau_z$

The resulting eigenvalues (*top*) and the cumulative energy contained in the first  $r$  modes (*bottom*) are shown in Fig. 3. It can be instantly noted that, in contrast to many textbook examples of POD, there is no large-scale organisation in the flow field responsible for a great portion of the fluctuating energy. On the contrary, the most energetic mode only accounts for 0.14% while the tenth mode still accounts for 0.11%. Yet, the modes stand out above the noise threshold and the mode shapes offer some insights into the flow physics.

Fig. 4 shows the first eight POD modes. Note that the modes are orthonormal by definition, so the corresponding eigenvalues are given in the title to indicate their relative strengths. The first two modes exhibit structures close to the end walls while the area around midspan shows relatively low amplitudes and rather noisy data. Mode 1 has larger amplitudes at the tip wall (positive  $z$ ) in both components of the wall shear stress while mode 2 shows a very similar structure basically mirrored at the  $z = 0$  plane. This corresponds to a periodic displacement of flow from the end walls into the channel and can be associated with an oscillation of the passage vortex (PV). The third mode is the first one to be dominated by structures associated with the KH instability in the separated shear layer around midspan. It is notable that the large amplitudes are only found close to midspan and are perfectly aligned with the  $z$  axis. Larger structures close to the end walls can still be seen here, yet at a lower

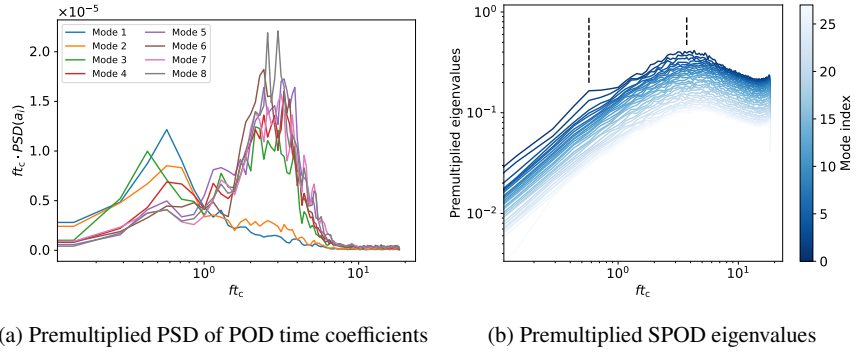


Fig. 5: Spectra for the MTU T161 without incoming wakes

amplitude compared to modes 1 and 2. A spanwise variation of the KH structures can be found in the following modes be it either in the form of a tilt (mode 4, 5, 8) or an inversion of the phase at some spanwise location (mode 6 and 7). All the modes featuring KH structures still show some amplitude at the end walls suggesting that these phenomena might be connected.

A look at the POD time coefficients, especially at their spectral content, can reveal additional information on the modes. Fig. 5 (a) shows the premultiplied Power Spectral Density (PSD) of the time coefficients for the first eight modes, obtained via (6), computed with Welch’s method with 256 samples per segment. Two distinct features can be identified: a low-frequency peak around 0.5 and a high frequency peak around 3. The first two modes, which do not show any sign of KH structures, clearly peak at the low frequency but show no contribution in the high frequency range. On the other hand, all modes with KH structures have the most significant contribution to the spectrum in this high frequency peak. While most of these modes do not show contributions above the noise level in the low frequency range, mode 3 is an exception: it features a low frequency peak in the same order of magnitude as modes 1 and 2. This suggests some connection of the oscillation of the secondary flow system with the KH shedding through this mode shape.

At this point, it can be helpful to resort to SPOD to be able to obtain optimal spatial modes corresponding to a single frequency. We use exactly the same dataset with weights chosen to represent a weighted 2-norm [16], a bin size of 256 and an overlap of 50%. Fig. 5 (b) shows the premultiplied SPOD spectrum with the area between mode 1 and 4 shaded in red to indicate the energy contained within the first three modes. The spectrum peaks in the same high frequency range as the POD time coefficient spectra discussed above. As expected from the above discussion of the POD, the separation between the first and second mode is not as clear as in many textbook examples. Nevertheless, the first three to four modes stand out in terms of separation between the modes and suggest that some kind of low-rank behaviour can possibly be identified [10]. We, therefore, examine the first four modes at the frequencies 0.57 and 3.72 in Fig. 6. The choice of former is due to the subtle low-



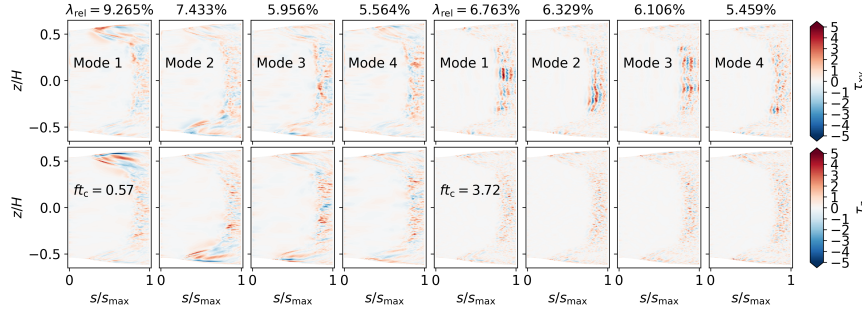
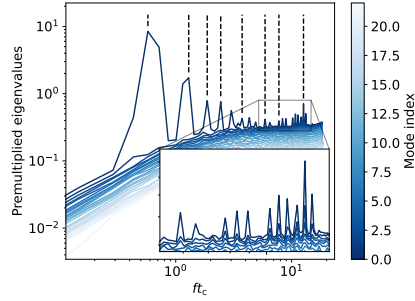


Fig. 6: MTU T161: First 4 SPOD modes for in-plane (*top*) and spanwise (*bottom*) wall shear stress  $\tau_{xy}$ ,  $\tau_z$  at  $ft_c = 0.57$  and  $3.71$

frequency peak while the latter is roughly the maximum premultiplied eigenvalue over all frequencies. Note, that slight changes to the investigated frequency do not qualitatively change the mode shapes in this case.

The first four columns show the first four modes of  $ft_c = 0.57$ . To present an indication for the energy of the respective mode, the mode eigenvalue  $\lambda_{rel}$  normalised with the sum over all eigenvalues at that frequency is given in the column header. The first two SPOD modes at  $ft_c = 0.57$  show a great resemblance with the first two POD modes, which is a consistent picture since the frequency analysis of the latter revealed that most of their energy is found at this low frequency. Looking at the higher modes, there is again some indication that the oscillation of the secondary flow system has an effect on the midspan flow, although the data in the separation bubble is rather noisy. In contrast to our argument above using the POD analysis, however, we see no direct connection with KH structures but a larger scale oscillation in the third mode. KH structures in the laminar separation bubble (LSB), on the other hand can be clearly identified in the in-plane wall shear stress for all modes at  $ft_c = 3.71$ . Similar to what was found above in the higher POD modes, the first mode at this frequency shows a vertical alignment of the KH structures while the higher modes introduce some tilting. The spanwise wall shear stress shows mainly turbulent noise. An interesting difference to the POD concerns the connection of the KH structures and the oscillation of the secondary flow system: while the POD suggested some combined mechanism through mode 3, the SPOD suggests that the two phenomena are, indeed, not directly coupled as no significant structures in the secondary flow region can be found at  $ft_c = 3.71$ . This underlines the importance of SPOD to avoid drawing false conclusions due to the missing frequency resolution of POD. It has to be mentioned, though, that the SPOD modes are rather noisy and for a more quantitative analysis, more samples in excess of the available 100 convective time units would be beneficial. Very recently, a sub-sampling method was suggested to overcome the problems associated with short time signals by sacrificing the high-frequency part of the spectrum to be able to obtain more realisations of low-frequency phenomena [17].

**Fig. 7** MTU T161: SPOD spectrum for the case with incoming wakes; frequencies for mode analysis marked with dashed lines



### 3.2 Blade row interaction

Besides the clean inflow configuration with freestream turbulence only, a dataset with incoming periodic disturbances generated by cylindrical wake generators was presented in [14]. POD was only used to obtain less noisy phase averages in the wake plane in this paper. In the following, we perform an SPOD analysis consistent with the one above. The dataset consists of 3009 samples, spanning 82 convective time units corresponding to 50 bar passes. Again, we use only every tenth sample of the original dataset sampled at 368 per  $t_c$ . The periodic wakes lead to an intermittently separated flow around midspan, which does not show any backflow on average [14].

The SPOD spectrum in Fig. 7 is dominated by the wake passing frequency  $ft_c = 0.61$  and its harmonics. Coincidentally, this frequency is very close to the one of the large-scale secondary flow oscillations found in the case without wakes. The higher harmonics are in a frequency range corresponding to the KH shedding. In the high frequency range  $ft_c > 5$ , another set of peaks standing out of the turbulent noise can be found which does not occur in the case without wakes. In the following, we will analyse the first modes at the frequencies marked with dashed lines. An inspection of the spectrum and the second modes revealed that these do not generally show larger scale structures with a significant signal to noise ratio.

Fig. 8 shows these modes, again along with their relative eigenvalue normalised with the sum of all eigenvalues at that frequency. Note that the ratio of the eigenvalues between different frequencies cannot be derived from these but must be obtained from Fig. 7. The first mode at  $ft_c = 0.58$  is clearly associated with the large-scale wake passing and is responsible for most of the energy at that frequency with mode 2 at  $\lambda_{\text{rel}} = 1.26\%$  only (not shown in the figure). Note that due to the choice of blocks and the time step size, the available frequencies in the SPOD only approximately match the bar passing frequency and its harmonics. The large structures in the in-plane wall shear stress describe the periodic separation and reattachment, although this conclusion can only be drawn in combination with knowledge about the local mean values. In contrast to the case without wakes, the oscillation of the corner separation appears to be dominated by the wake passing as seen in large coherent structures in the both wall shear stress components. The first three harmonics quickly decrease

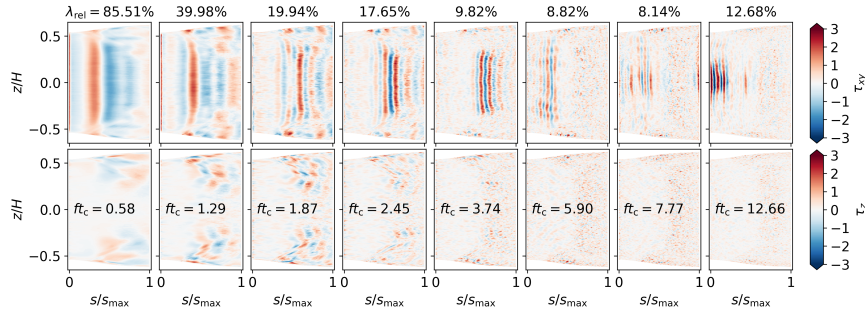


Fig. 8: MTU T161: First SPOD modes for in-plane (*top*) and spanwise (*bottom*) wall shear stress  $\tau_{xy}$ ,  $\tau_z$  at dominant frequencies

in eigenvalue and show refined structures corresponding to the same phenomenon. At frequencies in the range of the KH instability of the case without wakes, i.e.  $ft_c$  around 3, the characteristic vertical bands appear in the aft section of the blade. Again, from this frequency on, at best, a very subtle interaction with the secondary flow region can be identified.

When the frequency is further increased, another set of vertical structures with shorter wavelength can be found upstream, starting near the LE at  $ft_c = 12.66$ . The instantaneous flow field in a midspan plane (not shown) revealed, that these are the footprints of upstream traveling acoustic waves originating from the strong vortex shedding of the moving cylinder and their reflections from the adjacent blade pressure side. The high frequency structures near the LE could only be identified using the SPOD and cannot be observed in any of the first 30 POD modes. This, again, highlights the usefulness of the SPOD in distinguishing between different features of the flow which occur at different frequencies and are possibly hidden within high-energy low-frequency behaviour.

### 3.3 Shock wave boundary layer interaction

In this section, we analyse the modal content of the flow over a compressor cascade at transonic operating condition. The flow is simulated using a 4<sup>th</sup> order accurate LES based on a high-order DGSEM scheme. For a detailed description of the scheme, we refer to Bergmann *et al.* [4] and references therein. The linear cascade is computed based on a spanwise domain extrusion of 5% chord length, where periodic boundary conditions are applied along the pitchwise and the spanwise faces to approximate the flow over an infinite cascade of infinite blades. The computational domain consists of 2 276 829 hexahedral elements clustered around the blade and the shock location, adding to a total 145.7 million degrees of freedom per equation. The simulation is evaluated over 21 convective time units ( $t_c$ ) based on the chord length  $c$  and inflow

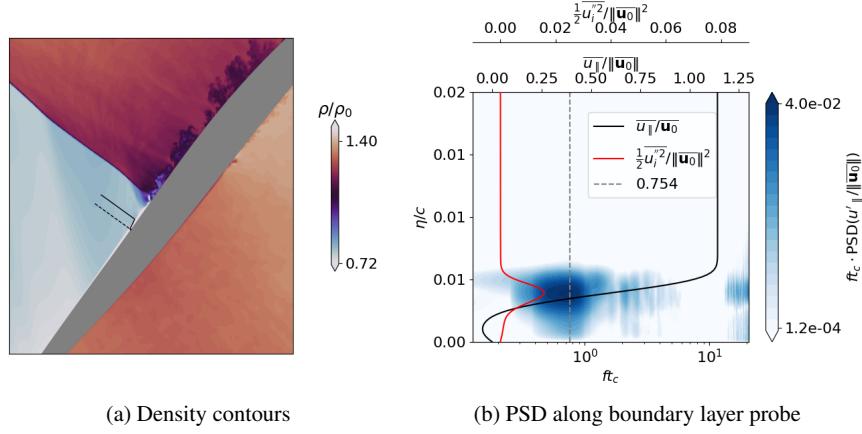


Fig. 9: DLR compressor cascade: (a) instantaneous density contours with boundary layer profile indicator in black; (b) contours of the frequency spectrum of  $u_{||}$  along the boundary layer with mean velocity and TKE profiles

velocity  $U_0$  and sampled at a non-dimensional frequency of 28 samples per time unit. We refer the interested reader to Klose *et al.* [11] for a more detailed description of the setup and discussion of the flow field for this testcase.

Given that the compressor cascade is at transonic operating conditions, the SPOD is computed based on the compressible energy norm [16] with input vector

$$\mathbf{X} = \left[ \rho', u'_{||}, u'_{\perp}, u'_z, T' \right]^T, \quad (11)$$

and weights

$$\mathbf{W} = \int_V \text{diag} \left( \frac{\bar{T}}{\gamma \bar{\rho} M_0^2}, \bar{\rho}, \bar{\rho}, \bar{\rho}, \frac{\bar{\rho}}{\gamma(\gamma-1)\bar{T}M_0^2} \right) dV, \quad (12)$$

where  $\rho$  is the density,  $T$  the temperature,  $u_i$  the velocity components and  $M$  the Mach number. All physical quantities here are non-dimensionalised with respect to reference quantities at the inlet measurement plane (indicated by subscript 0). A total of 568 snapshots are evaluated for the modal analysis for this testcase, where the bin size for the SPOD is 142 snapshots with 50% overlap.

The flow is characterized by an upstream laminar boundary layer, shock-induced separation and transition to turbulence. Features of the instantaneous flow field are shown in Fig. 9 (a), where contours of the density are shown at the mid-chord section of the blade around the shockwave and the premultiplied frequency spectrum of the wall-parallel velocity component  $u_{||}$  along a wall-normal probe is given in Fig. 9 (b). Additionally, the mean velocity and TKE profiles are indicated, as well as the peak in the spectrum at  $ft_c = 0.75$ . As shown by Klose *et al.* [11], low-amplitude

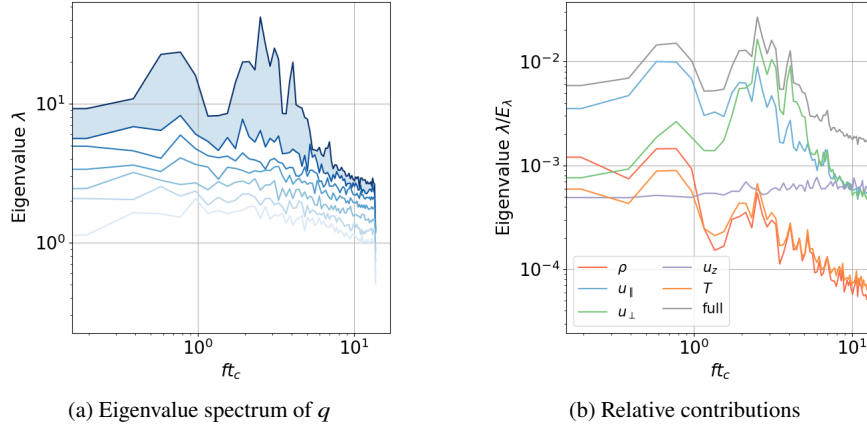


Fig. 10: DLR compressor cascade: (a) eigenvalue spectrum of  $q = [\rho, u_{\parallel}, u_{\perp}, u_z, T]$ ; (b) relative contributions to the first mode of the individual components of  $q$

oscillations of the normal shock occur in the range  $0.6 < ft_c < 0.8$ , as well as high-frequency fluctuations at  $ft_c = 2.6$ , which were associated with a wake mode.

The eigenvalue spectrum in Fig. 10(a) is obtained by computing the SPOD of the input vector (11) and the weights (12) as a whole, where the shaded area highlights the separation between the first and second SPOD modes. A distinctly separated peak occurs at  $ft_c = 0.77$  and a series of separated peaks at around  $ft_c = 2.52$ , closely matching the frequency peak along the boundary layer probe. To extract the contributions of each term to the overall fluctuating energy, the SPOD eigenvalues of the first mode for the individual components (with their respective weights) are shown in Fig. 10(b), together with the result of the *full* input vector. While the wall-parallel velocity component  $u'_{\parallel}$  dominates the energy in the lower frequency regime, the wall-normal component  $u'_{\perp}$  is the main contributor for the higher frequency peaks. The components measuring the compressibility effects ( $\rho'$ ,  $T'$ ) also predominantly contribute energy to the low-frequency modes, where they still only make up around 15% of the total energy.

The shape of the first SPOD mode for  $ft_c = 0.77$  and  $ft_c = 2.52$  for  $\rho'$ ,  $u'_{\parallel}$  and  $u'_{\perp}$  is given in Fig. 11. At  $ft_c = 0.77$ , the compression area upstream of the normal shock is distinctly highlighted by the density, where the thickening of the boundary layer is accompanied by a mild oblique compression wave. The movement of the normal shock itself is also tracked by the  $u'_{\parallel}$  velocity component and shows as a distinct, sharp mode structure normal to the blade surface. At the higher frequency of  $ft_c = 2.52$ , the shock wave is no longer discernible in the velocity components. Here,  $u'_{\perp}$  is dominant and its mode shape proves that the oscillating energy is almost exclusively contained in the wake.

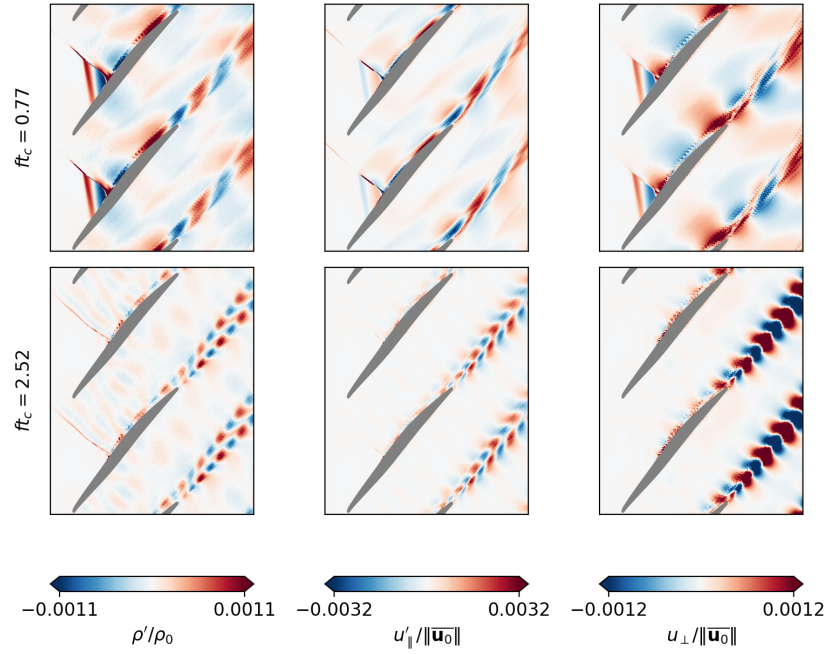


Fig. 11: DLR compressor cascade: First SPOD modes of the density (*left*), blade-parallel velocity (*middle*) and blade-normal velocity (*right*)

## 4 Conclusion

We have presented the application of two modal decomposition techniques, namely POD and SPOD, to previously published LES datasets of turbomachinery flows computed with our high-order DGSEM solver TRACE. While POD could be used to draw first conclusions even when large-scale effects did not dominate the turbulent spectrum in energy, the frequency resolution capabilities of SPOD allowed for a clearer analysis and separation of effects. In the LPT flow without incoming wakes, the weak but dominant feature was a low-frequency oscillation of the secondary flow system at time scales longer than a convective time unit. The SPOD showed that these oscillations were coupled with a large-scale motion of the LSB. We found, that the KH instability, occurring at higher frequencies was easy to detect and did not directly interact with the secondary flow system. An SPOD of the flow through the LPT with incoming wakes revealed the wakes' influence on the blade including the secondary flow system while the method was also able to detect the local KH mechanism in the intermittent separation bubble. It also revealed the footprint of

very high frequency acoustic perturbations, which originate from the vortex shedding of the upstream moving cylinder. In this case, "the frequency decomposition benefitted the analysis to reveal low-energy effects otherwise obscured by the dominant large-scale motion. Applied to the flow around a transonic compressor cascade, SPOD was able to discern two effects: first, low-frequency oscillations are associated with shock-wave boundary layer interaction and show higher contributions of compressible components to the total energy. Second, high-frequency oscillations are associated with vortex shedding in the wake in which compressibility does not play a significant role. It has to be noted, that many statements made in this paper depended on a combined analysis of modal decomposition techniques with other methods such as averages, frequency analysis, space-time diagrams or visualisation of the instantaneous flow field. In this respect, modal decomposition techniques are a valuable addition in the toolbox of unsteady flow analysis in turbomachinery flows.

## References

1. Alessandri, A., Bagnerini, P., Gaggero, M., Lengani, D., Simoni, D.: Dynamic mode decomposition for the inspection of three-regime separated transitional boundary layers using a least squares method. *Physics of Fluids* **31**(4), 044103 (2019). DOI 10.1063/1.5086225
2. The American Society of Mechanical Engineers: Unsteady Flow Interactions Between a High- and Low-Pressure Turbine: Part 2 — Rotor-Synchronic Averaging and Proper Orthogonal Decomposition of the Unsteady Flow Fields, *Turbo Expo: Power for Land, Sea, and Air*, vol. Volume 2A: Turbomachinery (2019). DOI 10.1115/GT2019-90824
3. The American Society of Mechanical Engineers: Proper Orthogonal Decomposition Analysis of Particle Image Velocimetry Data at the Inlet of a Centrifugal Compressor, *ASME International Mechanical Engineering Congress and Exposition*, vol. Volume 8: Fluids Engineering; Heat Transfer and Thermal Engineering (2022). DOI 10.1115/IMECE2022-94308
4. Bergmann, M., Morsbach, C., Klose, B.F., Ashcroft, G., Kügeler, E.: A numerical test rig for turbomachinery flows based on large eddy simulations with a high-order discontinuous Galerkin scheme - part 1: Sliding interfaces and unsteady row interactions. In: *Proceedings of ASME Turbo Expo 2023: Turbomachinery Technical Conference and Exposition*, GT2023-101623. Boston, MA, USA (2023)
5. Berkooz, G., Holmes, P., Lumley, J.L.: The proper orthogonal decomposition in the analysis of turbulent flows. *Annual Review of Fluid Mechanics* **25**(1), 539–575 (1993). DOI 10.1146/annurev.fl.25.010193.002543
6. Cizmas, P.G., Palacios, A.: Proper orthogonal decomposition of turbine rotor-stator interaction. *Journal of propulsion and power* **19**(2), 268–281 (2003)
7. Dotto, A., Lengani, D., Simoni, D., Tacchella, A.: Dynamic mode decomposition and Koopman spectral analysis of boundary layer separation-induced transition. *Physics of Fluids* **33**(10), 104104 (2021). DOI 10.1063/5.0065554
8. Feldhusen-Hoffmann, A., Lagemann, C., Loosen, S., Meysonnat, P., Klaas, M., Schröder, W.: Analysis of transonic buffet using dynamic mode decomposition. *Experiments in Fluids* **62**(4), 66 (2021). DOI 10.1007/s00348-020-03111-5
9. Fiore, M., Gojon, R., Sáez-Mischlich, G., Gressier, J.: Les of the t106 low-pressure turbine: Spectral proper orthogonal decomposition of the flow based on a fluctuating energy norm. *Computers & Fluids* **252**, 105761 (2023). DOI 10.1016/j.compfluid.2022.105761
10. He, X., Fang, Z., Rigas, G., Vahdati, M.: Spectral proper orthogonal decomposition of compressor tip leakage flow. *Physics of Fluids* **33**(10), 105105 (2021). DOI 10.1063/5.0065929

11. Klose, B.F., Morsbach, C., Bergmann, M., Hergt, A., Klinner, J., Grund, S., Kügeler, E.: A numerical test rig for turbomachinery flows based on large eddy simulations with a high-order discontinuous Galerkin scheme - part 2: Shock-capturing and transonic flows. In: Proceedings of ASME Turbo Expo 2023: Turbomachinery Technical Conference and Exposition, GT2023-101374. Boston, MA, USA (2023)
12. Lengani, D., Simoni, D., Ubaldi, M., Zunino, P., Bertini, F.: Experimental Investigation on the Time–Space Evolution of a Laminar Separation Bubble by Proper Orthogonal Decomposition and Dynamic Mode Decomposition. *Journal of Turbomachinery* **139**(3), 031006 (2016). DOI 10.1115/1.4034917
13. Mengaldo, G., Maulik, R.: PySPOD: A Python package for spectral proper orthogonal decomposition (SPOD). *Journal of Open Source Software* **6**(60), 2862 (2021). DOI 10.21105/joss.02862
14. Morsbach, C., Bergmann, M., Tosun, A., Klose, B.F., Bechlers, P., Kügeler, E.: A numerical test rig for turbomachinery flows based on large eddy simulations with a high-order discontinuous Galerkin scheme - part 3: Secondary flow effects. In: Proceedings of ASME Turbo Expo 2023: Turbomachinery Technical Conference and Exposition, GT2023-101374. Boston, MA, USA (2023)
15. Schmid, P.J.: Dynamic mode decomposition of numerical and experimental data. *Journal of Fluid Mechanics* **656**, 5–28 (2010). DOI 10.1017/S0022112010001217
16. Schmidt, O.T., Colonius, T.: Guide to spectral proper orthogonal decomposition. *AIAA Journal* **58**(3), 1023–1033 (2020). DOI 10.2514/1.J058809
17. Schneider, N., Köhler, S., von Wolfersdorf, J.: Experimental detection of organised motion in complex flows with modified spectral proper orthogonal decomposition. *Fluids* **8**(6), 184 (2023). DOI 10.3390/fluids8060184
18. Towne, A., Schmidt, O.T., Colonius, T.: Spectral proper orthogonal decomposition and its relationship to dynamic mode decomposition and resolvent analysis. *Journal of Fluid Mechanics* **847**, 821–867 (2018). DOI 10.1017/jfm.2018.283
19. Wang, R., He, X., Yan, X.: Spectral proper orthogonal decomposition analysis of trailing edge cutback film cooling flow. *Physics of Fluids* **34**(10), 105106 (2022). DOI 10.1063/5.0098796
20. Weiss, J.: A tutorial on the proper orthogonal decomposition. In: AIAA Aviation 2019 Forum. Dallas, Texas, USA (2019). DOI 10.2514/6.2019-3333

## Appendix

In the following, we will re-arrange (3) so that we can determine the POD modes and eigenvalues using an SVD of a weighted snapshot matrix. Inserting (2) into (3) yields

$$\left( \frac{\mathbf{X}\sqrt{\mathbf{W}}}{\sqrt{M-1}} \right)^H \frac{\mathbf{X}\sqrt{\mathbf{W}}}{\sqrt{M-1}} \boldsymbol{\Phi} = \boldsymbol{\Phi}\boldsymbol{\Lambda} \quad (13)$$

with  $\sqrt{\mathbf{W}} = \text{diag}(\sqrt{w_1}, \dots, \sqrt{w_N})$ . The weighted snapshot matrix can be written as compact SVD

$$\frac{\mathbf{X}\sqrt{\mathbf{W}}}{\sqrt{M-1}} = \mathbf{U}\boldsymbol{\Sigma}\mathbf{V}^H, \quad \mathbf{U} \in \mathbb{C}^{R \times R}, \boldsymbol{\Sigma} \in \mathbb{C}^{R \times R}, \mathbf{V} \in \mathbb{C}^{N \times R} \quad (14)$$

with  $R = \min(M, N)$  and  $\mathbf{U}^H\mathbf{U} = \mathbf{V}^H\mathbf{V} = \mathbf{1}$ . This yields

$$\mathbf{V}\boldsymbol{\Sigma}^H\boldsymbol{\Sigma}\mathbf{V}^H\boldsymbol{\Phi} = \boldsymbol{\Phi}\boldsymbol{\Lambda}. \quad (15)$$



With (4), it can be written as

$$\mathbf{V}\boldsymbol{\Sigma}^H\boldsymbol{\Sigma}\mathbf{V}^H = \sqrt{\mathbf{W}}\boldsymbol{\Phi}\boldsymbol{\Lambda}^H \left( \sqrt{\mathbf{W}}\boldsymbol{\Phi} \right)^H. \quad (16)$$

So the eigenvalues  $\boldsymbol{\Lambda}$  and modes  $\boldsymbol{\Phi}$  are obtained from the weighted snapshot SVD by

$$\boldsymbol{\Lambda} = \boldsymbol{\Lambda}^H = \boldsymbol{\Sigma}^H\boldsymbol{\Sigma} \quad (17)$$

$$\boldsymbol{\Phi} = \sqrt{\mathbf{W}^{-1}}\mathbf{V} \quad (18)$$

with  $\sqrt{\mathbf{W}^{-1}} = \text{diag} \left( \sqrt{w_1^{-1}}, \dots, \sqrt{w_N^{-1}} \right)$ .